Computer Simulations Reveal a Novel Nucleotide-Type Binding Orientation for Ellipticine-Based Anticancer c-kit Kinase Inhibitors[†]

Damien Thompson,*[,‡] Charlotte Miller,[§] and Florence O. McCarthy[§]

Tyndall National Institute, Lee Maltings, Cork, Ireland, and Department of Chemistry and School of Pharmacy, Analytical and Biological Chemistry Research Facility, University College Cork, Western Road, Cork, Ireland

Received July 1, 2008; Revised Manuscript Received July 25, 2008

ABSTRACT: Receptor tyrosine kinase (RTK) enzymes regulate cell signaling pathways and so are an important target for cancer chemotherapy. Current inhibitors of c-kit, a key RTK stem cell factor receptor, are inactive against the most common mutated variant Asp816Val, associated with highly malignant cancers. Recent combined experimental/simulation work has highlighted the utility of the ellipticine pharmacore in inhibiting mutant c-kit, and the present simulation study applies a combination of high-level simulation tools to probe further the binding of ellipticine-based derivatives to c-kit. We find a large preference for protonation of bound ellipticine, which stabilizes the negative protein residues that coordinated ADP·Mg^{2+} in the native complex. The resulting ellipticine inhibitor binding mode resembles the native nucleotide complex and serves to explain some existing experimental data on binding specificities, indicating that functionalization at the C4/C5 sites of ellipticine derivatives may be important for the design of novel nucleotide analogues that inhibit mutant c-kit.

Receptor tyrosine kinase (RTK)[1] enzymes are an attractive target for drug therapy, particularly cancer chemotherapy, as they regulate the signaling pathways that control cell growth and proliferation (*1*). c-kit, a stem cell factor (SCF) receptor, is one such RTK which plays a key role in mast cell survival, differentiation, maturation, and function (*2, 3*). The c-kit receptor is a transmembrane protein of the type III RTK subfamily and contains five extracellular immunoglobin-like domains, a juxtamembrane region, and a cytoplasmic catalytic domain. The intracellular domain exhibits tyrosine kinase activity; binding of SCF to c-kit activates its kinase activity via autophosphorylation on tyrosines located in the COOH-tail region (*2*−*4*), and downstream c-kit signaling involves a range of kinases and activators of transcription pathways that control cellular activities such as proliferation and apoptosis (*5*−*7*). Mutations in the gene encoding for c-kit are associated with highly malignant cancers, and mutated c-kit is therefore a viable drug target in anticancer chemotherapy (*8*−*18*). Current inhibitors of c-kit, including Gleevec, are inactive against the most common mutated variant Asp816Val. A recent publication, however, has documented the utility of the ellipticine pharmacophore in c-kit kinase inhibition and its ability to overcome this common mutated variant present in highly malignant tumors (*19*).

The ellipticine series of compounds (based on compound **1**, C9-OH ellipticine, in Figure 1) has well-known topoisomerase and anticancer activity. The kinase inhibitory activity of ellipticines is not particularly surprising given the structure of other known kinase inhibitors which have key hydroxycarbazole binding constituents (**2A** and **2B** in Figure 1, e.g., indolocarbazoles and phenylpyrrolocarbazoles) (*20, 21*). These compounds also have a key maleimide hydrogen-bonding group as part of their structure which interacts with the backbone of the protein. In the present work we model the c-kit inhibition of the ellipticines while introducing novel substituents to the tetracyclic structure in order to improve binding. From the recently described model (*19*) it would appear that the 5-methyl group (atom numbering is shown for compound **1** in Figure 1) points toward the protein backbone while the 11-methyl group points toward the solvent-exposed side of the binding pocket. The C9-OH group is also seen as a critical functionality (*19*).

The present work employs long molecular dynamics (MD) simulations to identify favorable binding orientations for a series of ellipticine-based compounds and then uses molecular dynamics free energy (MDFE) (*22*−*34*) simulations to compute binding free energy differences for ellipticine ligand **1** relative to the series of derivatives **3**−**10** shown in Figure 1. We focus on this particular series of ellipticine derivatives due to the availability of experimentally measured binding rates for **1** and **3**−**6** (*19*) and the potential for functionalization at the ellipticine methyl sites (**7**−**10**) which could improve binding. The MDFE simulation technique uses the vertical alchemical legs of the thermodynamic cycle in Figure 2 and has been extensively validated in recent years (see, for example, our recent work (*30*−*34*); see refs *29* and *35*

[†] This study has been supported by Science Foundation Ireland (SFI) under the Tyndall National Access Programme. Calculations were performed at Tyndall National Institute using in-house clusters provided by Science Foundation Ireland (SFI) and also at the SFI/HEA Irish Centre for High-End Computing (ICHEC).

* To whom correspondence should be addressed. E-mail: damien.thompson@tyndall.ie. Tel: +353214904327. Fax: +353214270271.

[‡] Tyndall National Institute.

[§] University College Cork.

[1] Abbreviations: RTK, receptor tyrosine kinase; SCF, stem cell factor; MD, molecular dynamics; MDFE, molecular dynamics free energy calculations; PBFE, Poisson−Boltzmann free energy calculations.

10.1021/bi801239u CCC: $40.75
Published on Web 08/29/2008

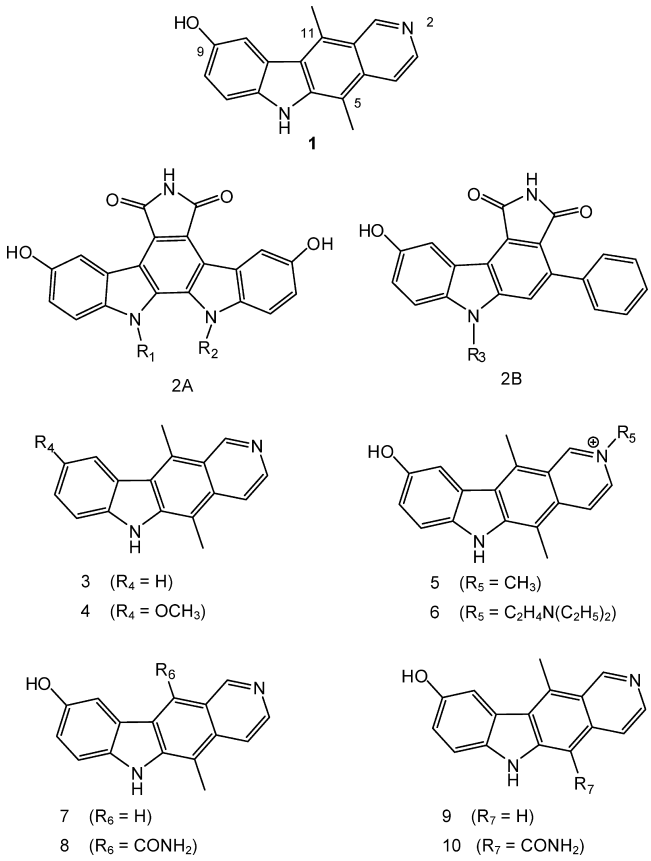

FIGURE 1: Ellipticine derivatives used to test the ligand discriminating capacity of c-kit tyrosine kinase.

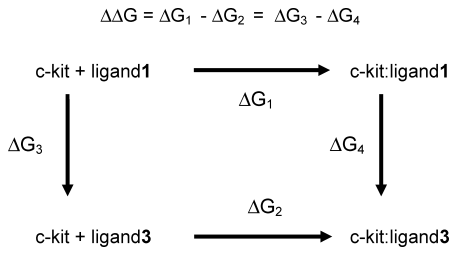

FIGURE 2: Thermodynamic cycle used for computation of the ellipticine-based ligand binding free energy differences $\Delta\Delta G$. ΔG_3 and ΔG_4 refer to free energy changes for ligand alchemical mutation in solution and in the c-kit tyrosine kinase, respectively, while ΔG_2 and ΔG_1 are free energy changes for ellipticine and ellipticine derivative C9-OH binding to c-kit, ligands **3** and **1**, respectively, in Figure 1. Similar cycles compare ellipticine and the other derivatives **4**−**10** shown in Figure 1.

for reviews), and we test it further in the present work by comparing our results to published measurements of ellipticine derivative binding rates (*19*). In contrast to the earlier (*19*) postulated binding mode based on (static) molecular mechanics calculations (orientation **E** in Figure 3), molecular dynamics finds a significant preference for a more ADP-like binding orientation. This ADP-like orientation is orientation **A** in Figure 3, and ellipticine binding to c-kit in orientation **A** is shown in Figure 4; all MD figures were prepared using Molscript (*36*) and rendered using Raster3D (*37*). Protonation of the ellipticine pyridine moiety aids this "nucleotide-type" orientation and leads to a significant computed binding penalty for functionalization at C11 (e.g., **8** in Figure 1 where $R_6 = CONH_2$) but not at C5 (e.g., **10** in Figure 1 where $R_7 = CONH_2$), in contrast to the binding behavior anticipated from the earlier binding pocket model (*19*). Understanding the impact of functionalization at these sites is an important step toward development of stronger binding ellipticine derivatives that will inhibit nucleotide binding to mutant c-kit RTK enzymes.

The following sections describe our Methods, Results, Discussion, and Conclusions. We show that the net negative electrostatic potential at one side of the c-kit pocket stabilizes the Mg^{2+} cation associated with ADP in the native complex and imposes also a "nucleotide-type" binding orientation on ellipticine derivatives; the ellipticine protonated N2 site plays a similar role to the ADP·Mg^{2+} cation, though the ellipticine binding level remains significantly below that of ADP.

METHODS

Molecular Dynamics Simulations. Starting structures were generated from a 2.9 Å human ADP−c-kit X-ray structure (*38*), PDB code 1PKG. This corresponds to the "active", nucleotide- and ellipticine-binding conformation of c-kit (*19, 38*). The Asp816Val mutation stabilizes this active conformation (*19*) but was not included explicitly in the c-kit model, given the ~20 Å distance between the Asp816 residue and the ligand binding site (*19, 38*). The ellipticine pharmacore was built in by overlaying ellipticine on ADP in the four possible orientations **A**−**D** shown in Figure 3 and then deleting the original ligand. Together with the predicted structure **E** from ref *19*, we thus consider five possible starting ellipticine conformations.

Model truncation and solvation followed closely the procedure used previously for simulations of amino acid binding to aminoacyl-tRNA synthetase proteins (*28*−*31, 33, 34, 39, 40*). Briefly, we considered protein residues within a 24 Å sphere centered on the N7-nitrogen of the ADP ligand of one monomer of the 1PKG dimer complex; N7 is one adenine nitrogen of the ring directly attached to the ribose, as labeled in Figure 3. Hydrogens were constructed with standard geometry. In addition to crystal waters, a large box of water was overlaid, and waters overlapping protein or beyond the 24 Å sphere were removed. The final model contained the ligand, 213 protein residues, and around 840 waters, including 3 crystal waters. Water and protein outside the 24 Å sphere were treated as a single, homogeneous dielectric medium with a dielectric constant of 80 (*41*). Atoms between 20 and 24 Å from the sphere center were harmonically restrained to their experimental positions, while dangling protein residues beyond 24 Å had their charges switched off. Though the sensitivity of the calculations to various model details (such as size of the protein sphere, simulation length) was not tested in the present work, it has been probed in a series of previous ligand−protein binding studies (*30, 39, 40*). Electrostatic interactions between atoms within the sphere were computed without any cutoff, using an efficient multipole approximation for distant groups (*42*). Van der Waals interactions were truncated at atomic separations of 13 Å. The position of the dielectric boundary between the inner sphere and the outer continuum was determined on-the-fly, by the position of the outermost water molecule. This procedure was shown to yield an exact reduction of the partition function of the whole system (*41*). A multipolar expansion with 20 terms was used to approximate the reaction field due to the surrounding continuum (*41*).

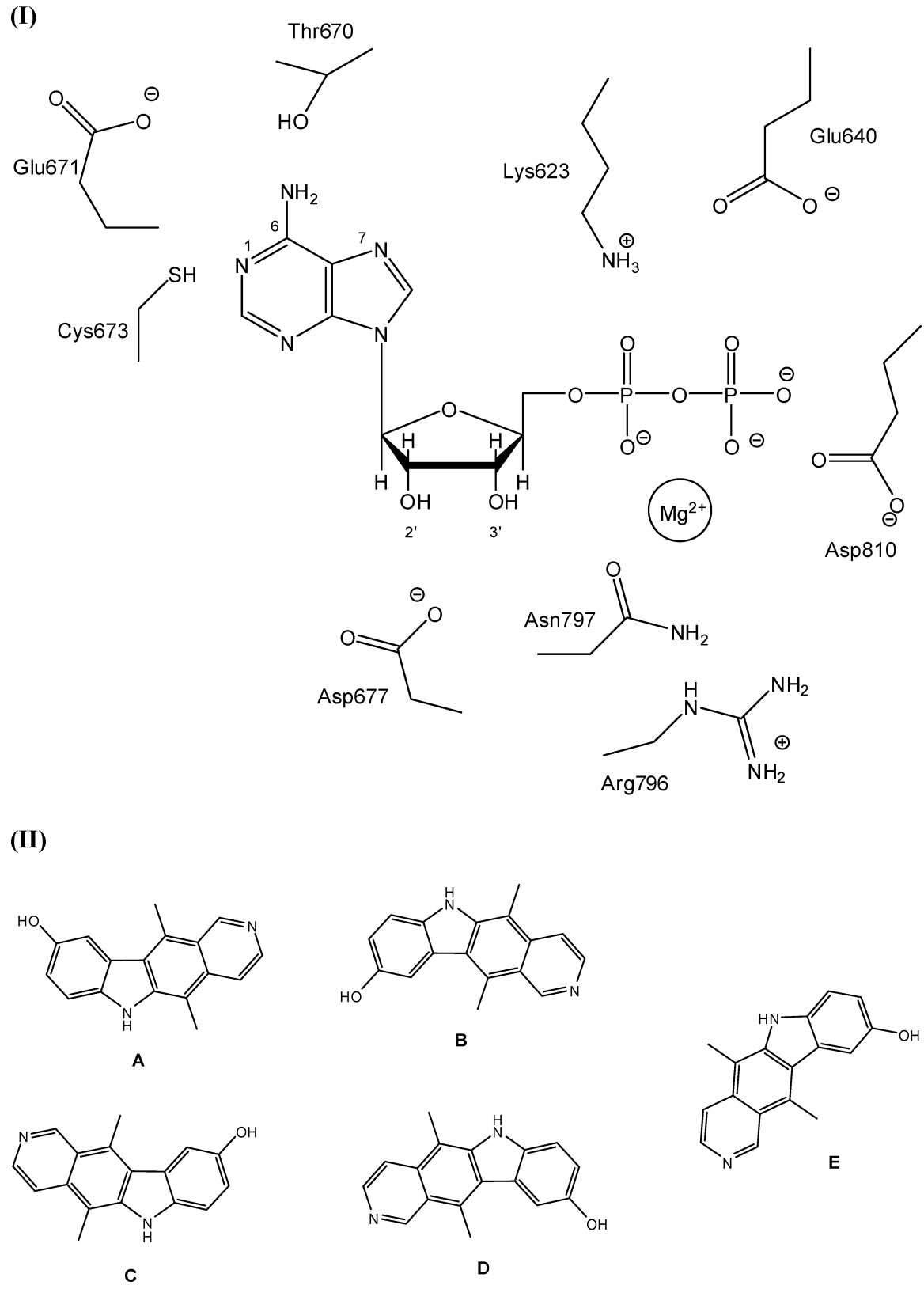

FIGURE 3: Panel I: Cartoon of the ADP·Mg^{2+} binding orientation from PDB structure 1PKG with nearby protein residue side chains shown. Note that residues Glu671, Cys673, and Arg796 stabilize ADP·Mg^{2+} binding largely through *backbone* (not shown) interactions. Panel II: Ellipticine MD starting orientations **1A**, **1B**, **1C**, and **1D** in the c-kit tyrosine kinase binding pocket, where the ellipticine center of mass is overlaid on the ADP center of mass, and the ADP ligand deleted, in each case. Orientation **1E** is **1D** rotated by approximately 300° clockwise and corresponds to the docked ellipticine−c-kit complex given in ref *19*.

The CHARMM force field (*43*) was used for protein, ADP, and Mg^{2+}, while new force field parameters were developed for the ellipticine-based inhibitors via *ab initio* electronic structure calculations using Gaussian03 (*44*), B3LYP/6-311++G** model chemistry (*45*), and a Natural Population Charge Analysis (*46*), as described in Supporting Information. A slightly modified TIP3P model was used for the water (*47*). Bonds involving hydrogen were constrained to their

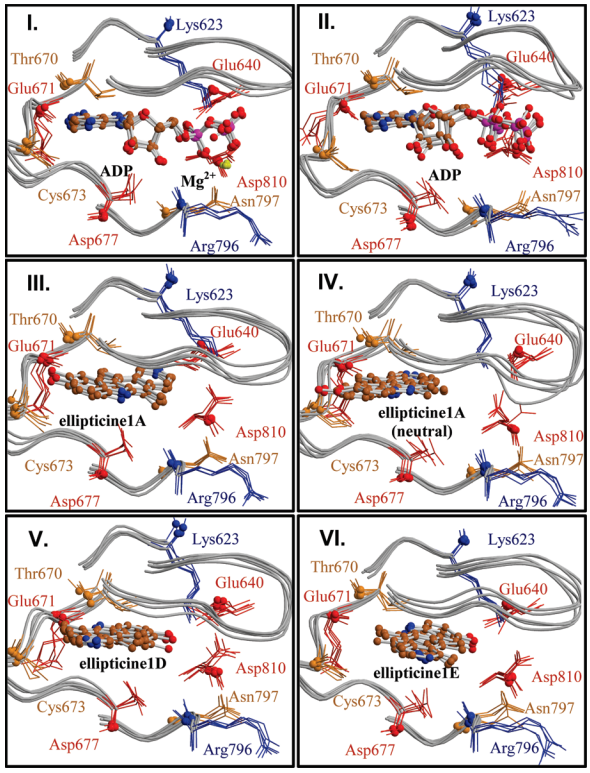

FIGURE 4: Five snapshots of the c-kit active site at 20 ps intervals from the last 80 ps of the MD trajectory. Panels show c-kit with bound (I) ADP·Mg^{2+}, (II) ADP alone with Mg^{2+} artificially removed, (III) ellipticine ligand **1** in orientation **A** (see Figures 1 and 3 above), (IV) ellipticine ligand **1** in orientation **A** with the N2 proton artificially removed, (V) ellipticine ligand **1** in orientation **D**, and (VI) ellipticine ligand **1** in orientation **E**. The ligand is shown in ball-and-stick representation. Protein residues forming the binding pocket are shown in tube representation. Important binding pocket residues are shown as sticks and colored according to charge: negative (red), positive (blue), and neutral (orange). The backbone amide carbon atom of each residue is shown as a sphere to guide the eye. Hydrogens are omitted for clarity. The ADP·Mg^{2+} cation is shown as a yellow sphere in panel I.

experimental lengths with the SHAKE algorithm (*48*), allowing the use of a 2 fs time step for dynamics.

Each complex was subjected to short minimization prior to molecular dynamics (MD) to remove any steric clashes. Two nanoseconds of MD was performed (for each complex) at constant room temperature and pressure. The first 200 ps of dynamics were used for thermalization and a gradual loosening of restraints toward the experimental c-kit tyrosine kinase crystal structure. Over the first 80 ps of equilibration, restraints were scaled from harmonic constraints with force constants of magnitude 5.0 kcal mol^{-1} $Å^{-1}$ $Å^{-1}$ on all solute non-hydrogen atoms to 1.0 kcal mol^{-1} $Å^{-1}$ $Å^{-1}$ on main chain protein non-hydrogen atoms. A further 120 ps of equilibration was then performed with very weak constraints of 0.2 kcal mol^{-1} $Å^{-1}$ $Å^{-1}$ on main chain protein non-hydrogen atoms. In all, approximately 80 ligand−c-kit MD simulations were performed, for ADP binding to c-kit, with and without its associated Mg^{2+} cation, and each ellipticine derivative **1** and **3**−**10** (Figure 1) binding to c-kit in five possible orientations **A**−**E** (Figure 3) and, where relevant, two possible protonation states (see pK_a calculations below). One nanosecond trajectories were also produced for each ligand in solution, **1** and **3**−**10** in Figure 1, solvated at the center of a 24 Å sphere of water molecules, with the ligand center of mass weakly restrained at the origin throughout the dynamics. We used the CHARMM program (*42*) version c31b2 for all calculations. Note that during the course of this work a molecular dynamics study of Gleevec binding to c-kit appeared (*49*), using a computational methodology very similar to that described above.

pK_a Calculations. To determine the protonation state of the ellipticine derivatives (Figure 1), we used Poisson−Boltzmann/Linear Response Approximation pK_a calculations to compare the free energy to protonate N2 (Figure 1) in the active site and in solution (*24, 30, 50*). The free energy to add a proton to the ligand is obtained from the expression (*50*) $\Delta G_{prot} = {}^1/_2\sum_i \Delta q_i (V_i^A + V_i^B)$. The sum is over the atoms of the pyridine ring which are not shared with the neighboring phenyl ring, i.e., positions 1−4 in **1** in Figure 1; electronic structure calculations described in Supporting Information show that only these atoms are significantly perturbed by protonation at N2. Δq_i is the shift in the atomic charge that occurs when the proton is added to the ligand and V_i^A (respectively, V_i^B) is the time-averaged electrostatic potential on atom i when the proton is absent (respectively, present). To obtain these potentials, we first performed MD simulations of the ligand−kinase complex (see above) in the two states of interest (proton present/absent). We then computed the electrostatic potential by numerically solving the Poisson equation of continuum electrostatics (using CHARMM), with the solvent treated as a dielectric continuum and the protein treated as a cavity. The same procedure is followed for the ligand alone in solution, yielding the free energy change ΔG_{solv}. The pK_a shift due to the protein environment is obtained from the double free energy difference: $\Delta\Delta G_H = \Delta G_{prot} - \Delta G_{solv} = 2.303kT(pK_{a,prot} - pK_{a,solv})$ where k is Boltzmann's constant and T the temperature. For each protonation state, Poisson calculations were performed for 250 structures sampled along the final 1.0 ns of 2.0 ns trajectories.

Free Energy Calculations. Poisson−Boltzmann free energy calculations (*39*) (PBFE) and alchemical free energy calculations (*22, 23*) (MDFE) were done to compute binding free energy differences between ligands with the methodology described earlier (*28*−*34, 39, 40, 51*). We employ the thermodynamic cycle given in Figure 2. We use the horizontal legs for simplified, Poisson−Boltzmann electrostatic free energy calculations (PBFE) and the vertical legs for more rigorous, alchemical, molecular dynamics free energy simulations (MDFE). In the latter, one ligand is reversibly transformed into another during a series of MD simulations; the potential energy function is mapped accordingly from one state to the other, and the corresponding work is derived from a thermodynamic integration formula (*28*).

Poisson−Boltzmann Free Energy (PBFE) Calculations. The electrostatic contribution to the ligand binding free energy is obtained by subtracting the electrostatic potential in the ligand−protein complex and in the separate ligand and protein (*39*). The electrostatic potential is obtained by numerically solving the Poisson−Boltzmann (PB) equation, using a cubic grid and a finite-difference algorithm implemented (*42*) in CHARMM. The structure of the ligand−protein complex is taken from the MD simulations (above). Calculations are performed for multiple structures, sampled every 4 ps along the last 1.0 ns of the trajectory, for a total of 250 structures; the computed binding free energies are

averaged over the ensemble. The separate ligand and protein structures are obtained by simply discarding the unwanted partner. Thus, structural relaxation on separating protein and ligand is not explicitly included (though it is implicit in the dielectric constant). The solvent dielectric constant was set to 80. The solute dielectric constant ϵ was set to 4, commonly used for protein active sites (*30*−*34, 39, 40, 50*−*, 54*); this empirical factor makes PBFE less rigorous than (the far more computationally demanding) MDFE, and so we use PBFE simply to estimate electrostatic binding energies for a given ligand in a series of different orientations rather than to compute the binding free energy difference between different ligands. The steric component of ligand binding energies was estimated by simply postprocessing the MD trajectories for the van der Waals ligand−protein interaction energies and taking an ensemble average over 250 structures (as above for the PBFE calculations).

Alchemical Molecular Dynamics Free Energy (MDFE) Simulations. The MDFE method transforms one ligand (e.g., **1** in Figure 1) into another (e.g., **3** in Figure 1) by gradually changing the C9 hydroxyl into a hydrogen, as shown in the vertical legs of the thermodynamic cycle given in Figure 2. To do this, the terms in the energy function associated with the C9-OH and C9-H are scaled respectively by $1 - \lambda$ and λ, where λ is a weight, or "coupling parameter" that varies gradually from zero to one, using the "PERT" module implemented in CHARMM (*42*). The successive weights used were $\lambda = 0.99$, 0.95, 0.9, 0.8, 0.6, 0.4, 0.2, 0.1, 0.05, and 0.01 for the starting ligand and $\lambda - 1$ for the competitor. The free energy derivative with respect to λ has the form $dG/d\lambda = \langle dU/d\lambda \rangle_\lambda$, where U is the energy function and the braces indicate an average over an MD simulation performed with a particular value of λ. The free energy derivatives were computed at each λ value from a 100 ps MD simulation (a "window"), where the first 40 ps was discarded as "equilibration" at the particular λ value. Each MDFE run thus corresponds to 1 ns. The derivative is integrated numerically to obtain ΔG, using trapezoidal integration except for van der Waals contributions close to the end points of the mutation ($\lambda = 0-0.03$ and $\lambda = 0.97-1$). For these end point contributions, the steepness of the derivative makes analytical integration more suitable (*55*). The procedure is applied to the protein−ligand complex and to the ligand alone in solution. Subtracting the two free energy changes gives $\Delta\Delta G$, the binding free energy difference between the two ligands (e.g., in Figure 2, ellipticine with and without the C9-OH group). To account for the dielectric heterogeneity of the region outside the simulation sphere, we follow the method of Simonson et al. (*55*): the final alchemical free energy change $\Delta\Delta G$ is corrected by adding the free energy to transform the homogeneous outer medium into a heterogeneous one. The correction is estimated by solving numerically the Poisson−Boltzmann equation using a dielectric constant of 1 for protein and 80 for solvent; see ref *55* for details. For the present system, the correction is always smaller than ± 1 kcal/mol and so is approximated as zero.

Free Energy Component Analysis. Since the energy function $U(\lambda)$ is a pairwise sum over individual groups (e.g., protein residues, water molecules) (*43*), the free energy derivative $dG/d\lambda$ and the free energy change ΔG can also be decomposed into group contributions (*56, 57*). Therefore, to identify active site residues contributing strongly to the overall free energy change, we used the free energy component analysis described earlier (*30*−*34, 39*). It is important to emphasize that these components are neither state functions nor experimentally measurable quantities. They depend on the details of the calculation; in particular, they are path-dependent (*56, 57*). In other words, they depend on the pathway that is followed between the initial and final states considered (which is defined by the λ dependency of $U(\lambda)$). Nevertheless, with certain precautions (see Results), these components can provide a rough, qualitative measure of each group's importance for the binding specificity.

The free energy component analysis allows a projection of the overall ΔG into interactions between each binding pocket group, P, and the (alchemically transformed) ligand S. All charges in the system are switched off except those on P and S. The electrostatic energy is computed and averaged over all the conformations sampled along each trajectory window i, corresponding to a particular value λ_i of the coupling parameter. Taking the difference between S = ligand 1 and S′ = ligand 2 gives the electrostatic contribution $dG_P/d\lambda$ of P to $dG/d\lambda$. Integrating from $\lambda_i = 0-1$ gives the electrostatic free energy component associated with P, similarly for van der Waals components, where atomic radii rather than charges are set to zero for all atoms except those on P and S (*32, 39*).

RESULTS

Structure, Dynamics, and Solvation of the ADP Binding Site in c-kit Tyrosine Kinase. ADP is a native ligand for c-kit and is thought to bind with one Mg^{2+} coligand (*38, 58*). We performed MD simulations of the ADP binding pocket, both with and without the Mg^{2+} cation, in an effort to understand the specificity of c-kit for ADP binding and the role of the Mg^{2+} cation in stabilizing ADP. The obtained structures and binding energetics (below) serve as a reference point for the non-native ellipticine ligand binding simulations and help to explain how the c-kit pocket stabilizes the protonated form of the ellipticine inhibitors.

Panels I and II of Figure 4 show overlays of five equally spaced snapshots from the last 80 ps of the ADP•Mg^{2+}•c-kit and ADP(no Mg^{2+})•c-kit MD trajectories (see Methods). These and all MD figures were prepared using Molscript (*36*) and rendered using Raster3D (*37*). ADP heavy-atom root-mean-square (rms) deviations (fluctuations) of 0.6 Å (0.3 Å) for ADP•Mg^{2+} (panel I of Figure 4) compared with 1.1 Å (0.4 Å) for ADP(no Mg^{2+}) (panel II of Figure 4), together with rms deviations (fluctuations) for protein heavy atoms within a 5 Å sphere of ADP of 0.8 Å (0.4 Å) and 1.0 Å (0.4 Å) for the ADP•Mg^{2+} and ADP(no Mg^{2+}) liganded complexes, respectively, indicate that the Mg^{2+} cation stabilizes the ADP binding site. Mg^{2+} has a very low rms fluctuation of just 0.3 Å over the 2 ns of dynamics. ADP•Mg^{2+} maintains the favorable binding pocket contacts seen in the starting X-ray structure (*38, 58*), sketched in Figure 3, with strong H-bonds present 90−100% of the time, namely, adenine N1−backbone amide Cys673, exocyclic N6−backbone amide Glu671, ribose sugar O2′ hydroxyl−side chain carboxylate Asp677, ribose sugar O3′−backbone amide Arg796, and α-phosphate−side chain ammonium Lys623. These are in addition to the weaker H-bonds (present 50−80% of the time) exocyclic N6−side chain hydroxyl Thr670, exocyclic

N6−side chain thiol Cys673, and β-phosphate−side chain ammonium Lys623 and steric packing with neutral residues lining the binding pocket (shown in tube representation in Figure 4).

The Mg^{2+} cation remains coordinated to one ADP α-phosphate, one ADP β-phosphate, one side chain carboxylate oxygen of Asp810, and the side chain amide oxygen of Asn797 over 2 ns of dynamics, and two ordered water molecules, conserved for the full 2 ns, complete its octahedral binding sphere. The strong Lys623−Glu640 salt bridge, together with the Phe811 (not shown) and Asp810 respective orientations away from and toward ADP·Mg^{2+}, noted in previous studies as important for binding pocket stability and activity (*58, 59*), are maintained throughout the MD simulations. ADP binding without Mg^{2+} on the other hand has much poorer electrostatic contacts, its diphosphate tail swinging toward solution to avoid electrostatic repulsion with Asp810 and, to a lesser extent, Glu640 (panel II of Figure 4, where the solvent-exposed side of the pocket is normal to and "above" the plane of Figure 4). As the diphosphate tail swings into the solvated region, it loses the α,β-phosphate−side chain ammonium Lys623 H-bonds after approximately 0.6 ns of free dynamics and a strong Lys623−Asp810 salt bridge forms. Asn797 and Glu640 find compensating interactions; the Asn797 side chain coordinates the Asp810 backbone amide and the Glu640 side chain coordinates the Asp810, Phe811, and Gly812 backbone amide groups. In contrast to the conserved water molecules coordinating Mg^{2+}, the ADP(no Mg^{2+}) diphosphate has coordinating waters exchanging rapidly, every 50−100 ps.

The computed Poisson−Boltzmann electrostatic binding energy (see Methods) of Mg^{2+} is −160 kcal/mol (data not shown), comparable to the Poisson−Boltzmann binding energies of the three Mg^{2+} cations in the ATP binding site of the aspartyl-tRNA synthetase protein (*60*) (approximately −100 to −140 kcal/mol (*31*)), in which all three Mg^{2+} cations have a population of essentially 100% (*31*). The Mg^{2+} cation associated with ADP in c-kit is thus very strongly bound; Mg^{2+} stabilizes the ADP binding site, offsetting the formally trinegative ADP ligand. Artificially switching the coordinating Asp810 atomic charges to those of Asn reduces the cation binding strength by ∼25% (data not shown). Though the ellipticine pharmacore is formally neutral in its nonionized form, the near-7 pK_a of N2 under physiological conditions (pK_a ∼ 7.4 (*61*), with ring H→CH_3 substitutions having a negligible effect, $\Delta pK_a < \pm 0.5$, on N2 pK_a (*61*)) and the negative residues in c-kit that stabilize the ADP Mg^{2+} cation promote the cationic N2−H^+ form in c-kit and significantly increase the binding strength of ellipticine, as described below.

Ellipticine Ionization State as a Function of Binding Orientation: $\Delta\Delta G$ for N2 Site Protonation. Table 1 shows computed pK_a shifts (see Methods) for ellipticine binding to c-kit in the five possible starting conformations **A**−**E** given in Figure 3. The ionization state of N2 depends strongly on the binding mode; orientation **A**, corresponding to a starting "nucleotide-type" binding mode (with N2 at the side of the pocket that stabilized Mg^{2+} in the ADP-bound complex), and orientation **E**, built from ref *19*, both have a very strong preference for the protonated form. Orientation **D** also has a strong preference for protonation at N2. These effective ellipticine pK_a values in c-kit can be explained from the MD structures. Structures in panels III, V, and VI of Figure 4 show how the N2−H^+ form is stabilized by negatively charged c-kit residues Glu640 (orientation **A**, panel III; the unpopulated neutral state in orientation **A** is given in panel IV for comparison) and Asp677 (orientations **D** and **E**, panels V and VI). Orientation **B** on the other hand favors the neutral form (Table 1) while orientation **C** has pK_a similar to that of ellipticine in solution (*61*). MD structures given in Supporting Information for **B** show the protonated N2-H^+ exposed to solvent and the unprotonated N2 coordinated to Lys623, hence the preference for the neutral form in orientation **B**, while **C** N2 forms weak interactions with the Glu671 backbone amide and Cys673 backbone amide in its protonated and neutral states, respectively. The favorability of N2 protonation for orientation **A** but not **B** (see below), together with the much stronger binding of **A** relative to **B**, illustrates the subtlety of the c-kit binding pocket and the need for dynamic simulations of inhibitor ionization and binding; a naive "placement" of ellipticine in the c-kit ADP binding site (Figure 3) would suggest that both orientations **A** and **B** would be conducive to "nucleotide-type" binding modes with the ellipticine N2 proton occupying a position similar to that of the ADP Mg^{2+} cation in the pocket.

Table 1: Computed C9-OH Ellipticine (Ligand **1** in Figure 1) N2 Protonation States in c-kit in a Range of Orientations[a]

starting orientation	ΔG_{sol}	ΔG_{prot}	$\Delta\Delta G$	pK_a shift	ellipticine state
A	−17.4	−26.4	−9.1	−6.7	charged
B	−17.4	−9.0	+8.4	+6.2	neutral
C	−17.4	−16.1	+1.3	+1.0	neutral/charged
D	−17.4	−22.5	−5.1	−3.8	charged
E	−17.4	−26.6	−9.2	−6.8	charged

[a] $\Delta\Delta G = \Delta G_{prot} - \Delta G_{sol}$ (in kcal/mol; see refs *50* and *30*). pK_a shifts are estimated from equilibrated MD structures, sampling every 4 ps along the final 1.0 ns of dynamics. Starting orientations **A**−**E** are given in Figure 3. The ellipticine charge state for each orientation is deduced from the pK_a shift and the pK_a of 7.4 (ref *61*) for ellipticine in solution under physiological conditions.

Ligand−c-kit Interaction Energies: Estimated ΔG for ADP, ADP·Mg^{2+}, and Ellipticine Inhibitor Binding. Table 2 gives ligand−c-kit interaction energies (see Methods) for the ellipticine series of compounds **1** and **3**−**10** shown in Figure 1. **8** (I) and **8** (II) denote two possible starting conformations for the amide $CONH_2$ group on carboxamide ligand **8**. Conformations **8** (I) and **8** (II) have respectively the amide oxygen pointing outward and inward relative to the plane of Figure 1, similarly for ligand **10**. To highlight the effect of changing orientation on interaction energy, the interaction energy ΔG for orientation **A** is set to zero in each case, and so $\Delta\Delta G$ values relative to orientation **A** are given. As expected, the native ADP·Mg^{2+} ligand is the most strongly bound, largely due to favorable electrostatic contacts with the c-kit binding pocket; in data not shown in Table 2, the ADP·Mg^{2+} total interaction energy is −67.8 kcal/mol, −35 kcal/mol better than ellipticine ligand **1**, and electrostatic interaction energy is −53.7 kcal/mol, −33 kcal/mol better than ellipticine ligand **1**. Artificially removing the Mg^{2+} cation has a dramatic effect on binding pocket dynamics (as described above) and also energetics, with total and electrostatic interaction energies reduced respectively to −40.6 and −20.7 kcal/mol (data not shown in Table 2); ADP loses 27 kcal/mol in overall binding energy, a balance between 6

Table 2: Ligand−c-kit Interaction Energies (kcal/mol) Relative to Orientation **A** with Ligands Numbered According to Figure 1 and in the Starting Orientations Shown in Figure 3[a]

	B/**C**^{0} (**C**$^+$)/**D**/**E** orientation	
ligand	change in total interaction energy $\Delta\Delta G$	change in electrostatic interaction energy $\Delta\Delta G$
1	+15.5/+14.2 (+11.4)/+13.1/+12.5	+15.6/+15.8 (+11.5)/+15.4/+11.6
3	+13.2/+11.2 (+13.0)/+9.5/+5.4	+18.1/+17.2 (+5.1)/+17.4/+13.7
4	+15.2/+14.4 (+13.7)/+11.9/+11.3	+15.3/+15.2 (+7.7)/+13.7/+9.8
5	+1.8/+11.1/+9.3/+9.2	+2.6/+7.2/+8.3/+9.4
6	+3.6/+2.9/+6.3/+4.1	+3.9/+4.3/+6.7/+3.7
7	+16.0/+10.8 (+11.4)/+9.7/+11.0	+18.4/+13.2 (+12.4)/+12.3/+12.3
8 (I)	+23.7/+13.4 (+12.0)/+14.6/+13.8	+21.2/+10.9 (+12.7)/+13.6/+14.2
8 (II)	+16.0/+16.8 (+7.3)/+17.8/+16.7	+16.3/+14.1 (+10.1)/+18.1/+17.1
9	+15.6/+11.6 (+12.5)/+11.3/+9.7	+15.7/+10.3 (+11.5)/+14.7/+13.3
10 (I)	+22.0/+13.6 (+15.3)/+13.4/+12.1	+20.3/+15.1 (+15.0)/+16.5/+15.7
10 (II)	+19.8/+14.6 (+12.5)/+12.4/+15.8	+19.9/+17.0 (+15.3)/+16.2/+18.0

[a] Ellipticine-based ligand charge states are as given in Table 1, i.e., charged for orientations **A**, **D**, and **E**, neutral for **B**, and both neutral and charged for **C** (**C**^{0} and **C**$^+$, respectively). Ellipticine derivatives **5** and **6** are permanent cations. **8** (I) and **8** (II) denote two possible starting orientations for the carboxamide $CONH_2$ group on ligand **8**; similarly for ligand **10**. Ligand−c-kit interaction energies (kcal/mol) are estimated from equilibrated MD structures, sampling every 4 ps along the final 1.0 ns of dynamics. Ellipticine orientation **A** interaction energy is set to zero in each case to highlight the change in interaction energy as a function of starting orientation, where a positive $\Delta\Delta G$ corresponds to preferential binding in orientation **A**. For each complex, the total interaction energy = the electrostatic ΔG (Poisson−Boltzmann ligand−c-kit electrostatic binding energy) + the steric ΔG (van der Waals ligand−c-kit interaction energy, not shown). Time-averaged standard deviations are 0.5−2.5 kcal/mol.

kcal/mol improvement in adenosine steric contacts and 33 kcal/mol loss in diphosphate electrostatic contacts. Interestingly, the loss of the cation puts ADP electrostatic binding at the same level as ellipticine, though improved steric contacts gives ADP an overall binding energy approximately 10 kcal/mol better than ellipticine, even with the cation artificially removed, highlighting the need to "build" on the core ellipticine pharmacore to increase its binding strength, e.g., toward compounds of type **2A** and **2B** in Figure 1.

The most important result from the binding data in Table 2 is that orientation **A** is significantly favored for all of the ellipticine derivatives **1** and **3**−**10**, with moderate time-averaged standard deviations of 0.5−2.5 kcal/mol in the computed $\Delta\Delta G$ values. Control simulations reported in Supporting Information indicate that the "removal" of the N2 site via replacement of the ionizable pyridine group with a nonionizable phenyl group (ligand **11**) removes this strong preference for orientation **A**. Figure 4 shows the different binding interactions used for ADP and ellipticine, and below, an attempt is made to highlight residues crucial for distinguishing between ellipticine derivatives, using a free energy component analysis.

Computed Binding Specificities for a Range of Ellipticine-Based Compounds. The importance of various c-kit binding pocket residues for binding ADP and ATP nucleotides and inhibitors such as SU6597 and STI571 (Gleevec) have been highlighted in earlier X-ray (*38, 58*) and (static) molecular mechanics "docking" studies (*19, 59, 62, 63*). In addition, molecular dynamics simulations have been very recently used to design a more active, less toxic Gleevec derivative for c-kit inhibition (*49*). While these studies, together with the above analysis based on Poisson−Boltzmann electrostatic energies and van der Waals interaction energies, are useful for identifying stable binding modes and serve as an important step toward a more quantitative understanding of c-kit discrimination, the much more expensive alchemical molecular dynamics free energy (MDFE) calculations (see Methods), which automatically cancel out any changes in binding pocket energetics not directly attributable to ligand discrimination, are necessary to obtain highly accurate ligand binding free energy differences $\Delta\Delta G$. Only ligands which bind in similar orientations may be compared using MDFE; crucially, Table 2 shows that all the ellipticine derivatives **1** and **3**−**10** (Figure 1) show a significant preference for binding in orientation **A** (Figure 2), and so we use MDFE to calculate the discriminating capacity of the c-kit pocket for ellipticine functionalization and identify promising derivatives for c-kit inhibition.

Table 3 gives calculated MDFE $\Delta\Delta G$ binding free energy differences for competitive ligand binding to c-kit, comparing ligand **1** with ligands **3**−**10**. All calculations used the most stable orientation **A**, with one exception: to test the strength of the putative ellipticine C9-OH−Glu640/Lys623 interaction (*19*), ligand **1** vs ligand **3** was also tested using the next most stable orientation, **E** built from ref *19*.

*Inhibitor **1** vs **3** and **1** vs **4** Competitive Binding: $\Delta\Delta G$ for Removal and Methylation of the Ellipticine C9-OH Group.* For ligand **1** vs **3** we compute a binding free energy difference of +2.1 kcal/mol in favor of ligand **1** binding. All MDFE runs reported in Table 3 were initiated from independent starting points taken at 0.5 ns intervals along the native 1.0 ns solution and 2.0 ns protein MD trajectories and show no consistent dependence on starting point. Standard deviations computed over the eight independent protein runs in each case range from 0.5 to 4.5 kcal/mol and are typically ∼60% of the computed binding free energy difference $\Delta\Delta G$, similar to earlier studies (*30*−*34*). The removal of the hydroxyl group at C9, substituting OH (ligand **1**) for H (ligand **3**), destabilizes the ligand, the magnitude of $\Delta\Delta G$ indicating that ligand **1** will have a substantially higher binding strength than ligand **3**, in agreement with the kinetic data in ref *19*, which reports IC_{50} values of 0.4 and >10 μM for ligand **1** and **3**, respectively (our numbering, from Figure 1; note a different ligand numbering scheme is used in ref *19*). Thus, the ellipticine ligand **1** with a hydroxyl group at C9 (C9-OH ellipticine) is a better inhibitor of c-kit than the nonhydroxylated analogue **3** (unfunctionalised ellipticine); the electrostatic and van der Waals contributions to $\Delta\Delta G$ given in Table 3 and the free energy components in Table 4 show that the beneficial effect of the C9-OH group is almost predominantly due to its favorable electrostatic interactions with c-kit pocket residue Cys673.

Table 3: MDFE Alchemical Free Energy Changes ΔG in Solution and in c-kit for Competitive Binding of Ellipticine Derivatives[a]

ligand	ΔG in solution	ΔG in c-kit	$\Delta\Delta G$	$\Delta\Delta G_{\text{electrostatic}}$	$\Delta\Delta G_{\text{van der Waals}}$
1 vs **3**	+20.5, +20.5/+20.5, +20.6	+22.9, +22.7, +22.3, +22.6/+22.9, +22.8, +22.6, +22.3	+2.1 (1.0)	+1.9 (1.0)	+0.2 (0.4)
1 vs **4**	+13.5, +13.5/+13.9, +13.9	+13.8, +14.5, +15.1, +15.3/+15.3, +15.4, +14.6, +15.5	+1.2 (0.8)	−0.3 (0.1)	+1.5 (0.9)
1 vs **3** (*)	+20.5, +20.5/+20.5, +20.6	+22.0, +16.1, +15.3, +20.4/+23.4, +21.4, +22.5, +22.0	−0.1 (2.4)	+1.7 (1.9)	−1.8 (2.1)
1 vs **5**	+19.2, +19.3/+20.6, +20.2	+20.0, +18.7, +20.0, +19.3/+20.3, +18.3, +18.3, +18.5	−0.7 (0.8)	+0.1 (0.1)	−0.8 (0.8)
1 vs **6**	+3.8, +3.3/+4.7, +4.5	+16.1, +11.3, +13.8, +12.9/+12.0, +11.6, +9.7, +13.4	+8.5 (4.5)	+0.5 (0.6)	+8.0 (4.4)
1 vs **7**	−4.1, −4.0/−3.3, −3.2	−3.5, −3.8, −4.1, −3.9/−3.1, −3.2, −3.0, −2.6	+0.3 (0.5)	−0.1 (0.1)	+0.4 (0.5)
1 vs **8** (I)	−49.2, −46.9/−48.3, −48.2	−45.2, −45.6, −42.3, −42.2/−45.3, −45.6, −46.2, −47.1	+3.2 (2.2)	+3.0 (2.0)	+0.2 (0.8)
1 vs **8** (II)	−49.2, −46.9/−48.3, −48.2	−42.2, −40.7, −39.0, −46.4/−47.8, −46.0, −44.8, −46.4	+4.0 (3.2)	+4.0 (2.9)	0.0 (0.8)
1 vs **9**	−20.7, −20.8/−20.2, −20.4	−20.3, −20.1, −20.0, −19.7/−19.9, −19.4, −19.6, −19.5	+0.7 (0.5)	−0.1 (0.0)	+0.8 (0.5)
1 vs **10** (I)	−64.0, −64.2/−63.2, −62.9	−63.4, −63.4, −63.6, −64.3/−64.6, −63.9, −63.4, −63.2	−0.1 (0.5)	+0.3 (0.5)	−0.4 (0.5)
1 vs **10** (II)	−64.0, −64.2/−63.2, −62.9	−63.4, −62.7, −63.7, −63.2/−63.9, −63.8, −62.5, −62.7	+0.3 (0.6)	+0.4 (0.5)	−0.1 (0.5)

[a] Ligands numbered according to Figure 1. In kcal/mol. All runs are for ligand orientation **A**, except (*) which is for ligand orientation **E** (Figure 3). A positive $\Delta\Delta G$ corresponds to preferential binding of ligand **1**. "Forward" runs transform ligand **1** into the competitor ligand and are listed before the slash; "backward" runs transform the competitor into ligand **1** and are listed after the slash. **8** (I) and **8** (II) refer to ligand **8** in two alternative starting carboxamide orientations; similarly for ligand **10**. $\Delta\Delta G$ values are averages over the runs shown with standard deviations in parentheses. Runs were initiated from independent starting points taken at 0.5 ns intervals along the native 1.0 ns solution and 2.0 ns protein MD trajectories. Electrostatic and van der Waals contributions are also shown (last columns).

Table 4: MDFE Free Energy Components $\Delta\Delta G$ for Competitive Binding of Ellipticine Derivatives[a]

ligand	$\Delta\Delta G_{\text{electrostatic}}$ components	$\Delta\Delta G_{\text{van der Waals}}$ components
1 vs **3**	ligand = +0.8; water = −0.8; protein = +6.0 Cys673 = +5.4 (+5.4; 90%)	N/A
1 vs **4**	N/A	ligand = +0.3; water = +0.6; protein = +0.6 Cys673 = +0.6 (+0.6; 104%)
1 vs **3** (*)	ligand = +0.6; water = −0.8; protein = +4.9 Lys623 = +8.3; Glu640 = −0.2; Cys809 = +1.2; Asp810 = −0.9; Phe811 = 0.2 (4.6; 93%)	ligand = +0.1; water = +0.2; protein = −0.1 Lys623 = −0.7; Glu640 = −0.8; Cys809 = −0.4; Asp810 = −0.5; Phe811 = −0.2 (−0.5; 117%)
1 vs **5**	N/A	ligand = +0.0; water = −0.2; protein = +1.5 Lys623 = −0.5; Glu640 = +3.1; Cys809 = +0.2; Asp810 = −0.4; Phe811 = −0.2 (+2.3; 155%)
1 vs **6**	N/A	ligand = +0.5; water = +2.2; protein = +5.4 Lys623 = +0.6; Glu640 = +3.3; Leu644 = +1.1; Val668 = +1.6; Ile669 = −0.6; Thr670 = 2.3; Cys809 = +0.2; Asp810 = −0.4; Phe811 = −0.2 (+8.1; 150%)
1 vs **7**	N/A	ligand = +0.4; water = −0.5; protein = +0.4 Val603 = +0.2; Ala621 = +0.1; Val654 =+0.2; Thr670 = −0.5; Leu799 = +0.2; Cys809 = +0.2 (+0.4; 104%)
1 vs **8** (I)	ligand = +0.4; water = +5.6; protein = −0.1 Val603 = −0.5; Ala621 = −0.1; Val654 = +0.2; Thr670 = −0.7; Leu799 = +0.2; Cys809 = +0.3 (−0.4; 70%)	N/A
1 vs 9	N/A	ligand = −0.1; water = −0.1; protein = +0.9 Gly596 = +0.2; Val603 = +0.3; Leu799 = +0.4; Cys809 = +0.2 (1.1; 119%)

[a] Components calculated from one run in each direction. Ligands numbered according to Figure 1. MDFE free energy components in kcal/mol. Components are given for residues within 5 Å of the ligand for at least 75% of the trajectory. See legend for details of MDFE runs. N/A indicates a negligible electrostatic or steric contribution to the total $\Delta\Delta G$, as given in Table 3. For carboxamide ligand **8** components are calculated for only the most stable amide orientation, orientation I, as deduced from the $\Delta\Delta G$ values in Table 3. The values in parentheses in each case give the sum of the individual residues listed, together with the percentage this represents of the overall protein component.

Competitive binding of ligands **1** and **4** on the other hand gives a lower predicted binding free energy difference $\Delta\Delta G$ of +1.2 kcal/mol, again in agreement with the kinetic data (*19*) which indicated that the C9-OCH_3 analogue **4** is intermediate in binding strength between **1** (C9-OH) and **3** (C9-H). Binding dynamics for ligands **3** and **4** is described in Supporting Information; both **3** and **4** lose the favorable interaction with the Cys673 backbone amide. For **1** vs **4**, however, the difference in binding strength is primarily due to inferior *steric* contacts for the methoxylated ligand **4** ($\Delta\Delta G_{\text{van der Waals}}$ = +1.5 kcal/mol, Table 3), with Cys673 (Table 4) preferring the smaller OH group.

Interestingly, repeating the **1** vs **3** MDFE simulations with the alternative ligand orientation **E** (Figure 3) gives $\Delta\Delta G$ of approximately zero (Table 3), the electrostatic stabilization of C9-OH by Lys623 (Table 4), offset by unfavorable steric contacts with the binding pocket, particularly residues Glu640, Lys623, Asp810, and Cys809 (Table 4). Thus, in this case, orientation **A** (the most stable predicted ellipticine binding mode found by molecular dynamics, Table 2), but not orientation **E** (the structure predicted from less rigorous docking simulations (*19*)), gives predicted binding specificity in line with kinetic binding assays (*19*).

*Inhibitor **1** vs **5** and **1** vs **6** Competitive Binding: $\Delta\Delta G$ for Functionalization of the N2 Site.* Simulations testing the tolerance for functionalization of N2 with bulky organic groups CH_3 (ligand **5**) and $C_2H_4N(C_2H_5)_2$ (ligand **6**) gave MDFE $\Delta\Delta G$ values of −0.7 kcal/mol in favor of **5** for **1** vs **5** binding and +8.5 kcal/mol in favor of **1** for **1** vs **6** binding, with steric effects predominating as expected (Table 3). The stable binding modes found for ligands **5** and **6** in orientation **A** are given in Supporting Information; in spite of the bulky group on N2, orientation **A** remains the most favorable binding orientation for ellipticine analogues **5** and **6** (Table 2), though the degree of preference for orientation **A** is lowered substantially compared to the **A** preference expressed

by the other ellipticine derivatives (Table 2). The similar computed binding strengths of **1** and **5** ($\Delta\Delta G = -0.7$ kcal/mol, Table 3) are in agreement with their equivalent measured IC_{50} values (*19*). The slightly *improved* van der Waals interactions for ligand **5** are interesting ($\Delta\Delta G_{\text{van der Waals}}$ for **1** vs **5** $= -0.8$ kcal/mol, Table 3); MD structures given in Supporting Information and the free energy components in Table 4 show that the $N2^{+}$-CH_3−Glu640 steric clash is offset by improved solvation, giving the (small) net negative steric $\Delta\Delta G$ in favor of ligand **5**.

Far more surprising than the computed preference (Table 2) of ligand **5** for orientation **A** is the preference of ligand **6** for orientation **A** relative to orientations **D** or **E**, which have the bulky $C_2H_4N(C_2H_5)_2$ group at N2 exposed to solvent rather than buried in the c-kit pocket (Figure 3). For both orientations **D** and **E**, however, molecular dynamics shows that ligand **6** shifts significantly in the c-kit binding pocket, as described in Supporting Information, with concomitant reduction in binding energy relative to orientation **A** in which the core ellipticine moiety of ligand **6** maintains the same favorable interactions as ligand **1**. This "drifting" of **6** in orientations **D** and **E** was observed over multiple simulations, including those initiated with **6** in orientation **D** rotated by ±10° and orientation **E** initiated from well-equilibrated structures of **1** in orientation **E** with the $C_2H_4N(C_2H_5)_2$ group "built in" and the complex resolvated and equilibrated (data not shown). Thus **A** is the most favorable orientation we found for ligand **6**, with loss of core ellipticine contacts with the c-kit pocket and poor solvation of the bulky organic group penalizing the sterically more amenable orientations **D** and **E**. Interestingly, orientation **E** is punished relative to orientation **A** to a lesser degree for ligand **6** than for the other smaller ellipticine derivatives (Table 2); the bulky C_2H_4N-$(C_2H_5)_2$ group on N2 in ligand **6** actually helps to stabilize orientation **E**, as described in Supporting Information, maintaining a good electrostatic contact between the C9-OH and a negative binding pocket residue, in this case Asp810 as distinct from Glu640 in the earlier postulated model (*19*).

MDFE simulations for competitive binding of **1** vs **6** reveal the expected severe van der Waals penalty due to the buried bulky $C_2H_4N(C_2H_5)_2$ group, $\Delta\Delta G = +8.5$ kcal/mol in favor of ligand **1** binding (Table 3). Steric clashes with residues Glu640, Thr670, Val668, Leu644, and Lys623 severely penalize **6** (Table 4). This is in stark contrast to the near-equivalent measured IC_{50} values for ligands **1** and **6** (*19*), indicating that (a) we did not scan the conformational space in the c-kit pocket sufficiently well to find the true **6** binding mode (we limited ourselves to the five starting conformations shown in Figure 2), (b) we did not run sufficiently long simulations to allow large-scale conformational change to occur and "open up" space for **6** in orientation **A** (we ran 2.0 ns MD simulations for each ligand in each orientation and a total of eight 1.0 ns MDFE **1** vs **6** competitive binding simulations), or (c) there was some other artifact in the simulations and/or experiments (*19*).

*Inhibitor **1** vs **7**, **1** vs **8**, **1** vs **9**, and **1** vs **10** Competitive Binding: $\Delta\Delta G$ for Removal and Functionalization of the C11 and C5 Methyl Groups.* Having compared our computed MDFE $\Delta\Delta G$ values to available experimental measurements (*19*), we then tested the tolerance of the c-kit pocket for removal, and functionalization, of the ellipticine methyl groups. Ligands **7** and **8** in Figure 1 have the CH_3 on C11 switched to H and $CONH_2$, respectively, while ligands **9** and **10** have the CH_3 on C5 switched to H and $CONH_2$, respectively. Hence ligands **7** and **9** are isomers and have the methyl group removed, while ligands **9** and **10** are also isomers but have the methyl group replaced with an amide. Results shown in Table 2 indicate that, in all cases, orientation **A** remains the preferred binding orientation and so site C11 is buried in the c-kit pocket while site C5 is more solvent-exposed. MDFE data in Table 3 reveal a significant binding penalty for functionalization at C11 but not C5, which has important consequences for the design of more effective ellipticine-based pharmacores, as discussed below.

Simply removing the methyl group at both C11 and C5 gives a negligible change in binding energy ($\Delta\Delta G$ **1** vs **7** $= +0.3$ kcal/mol, $\Delta\Delta G$ **1** vs **9** $= +0.7$ kcal/mol), with just a small steric preference for the methyl group (Table 3). Free energy components in Table 4 for **1** vs **7** show that Thr670 favors the removal of the methyl group at C11, but this slight preference for ligand **7** is outweighed by the favorable steric contacts between the methyl group of **1** and other nearby residues, giving a net protein steric component of +0.4 kcal/mol favoring ligand **1**. Similarly for **1** vs **9**, the slight steric stabilization of the methyl group by nearby protein residues (Table 4) gives an overall $\Delta\Delta G$ of just +0.7 kcal/mol (Table 3). Interestingly, water appears to exert a larger influence on binding specificity for the more "buried" ligand **7** (Table 4), though the numbers involved are very small, ≤0.5 kcal/mol.

Figure 5 shows the binding modes of ligands **8** and **10**, with amide groups built on "buried" C11 and the more solvent-exposed C5, respectively. Table 3 quantifies the penalization of carboxamide derivative **8** relative to ligand **1**, with a computed $\Delta\Delta G$ of at least +3.2 kcal/mol in favor of **1**. Free energy components in Table 4 show that the protein contribution that favors **8** is outweighed by the water component in favor of **1**; the new amide group is stabilized electrostatically by Thr670 (Figure 5 and Table 4), but this is offset by a significant electrostatic water penalty for "burying" the amide group in the protein pocket (Table 4), to give the net $\Delta\Delta G$ values of +3.2 and +4.0 kcal/mol in favor of ligand **1** for the two starting amide conformations I and II (Table 3). Functionalizing the more solvent-exposed C5 site on the other hand does not significantly penalize binding, as shown by the **1** vs **10** MDFE data in Table 3. In the preferred orientation I, the new amide group on ligand **10** has essentially no binding free energy difference relative to **1**. Note that this penalization of functionalization at C11 but not C5 is precisely the opposite of what one would anticipate for orientation **E** (*19*), which is rotated clockwise by 120° (Figure 3) relative to the most favorable binding orientation **A**.

DISCUSSION

Role of Positive Charge in Ligand Binding to c-kit Tyrosine Kinase. The crucial importance of ligand−protein active site charge balancing is illustrated in the present study by the large change in ligand binding energies associated with the addition/removal of ligand positive charge in the Glu640-Lys623-Asp810 region of the c-kit binding pocket.

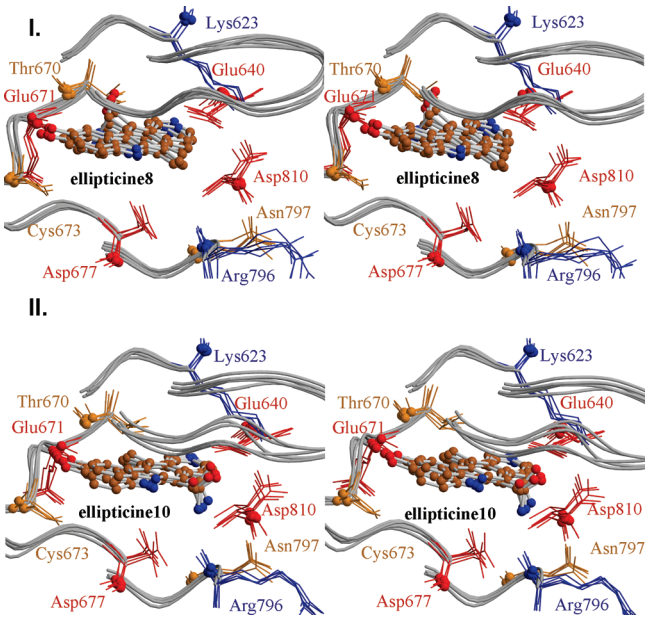

FIGURE 5: Five snapshots of the c-kit active site at 20 ps intervals from the last 80 ps of the MD trajectory. Panels show cross-eyed stereoviews of c-kit with bound carboxamide ligands; panel I shows ligand **8** and panel II shows ligand **10** (see Figure 1 above for ligand numbering). The ligand is shown in ball-and-stick representation. Protein residues forming the binding pocket are shown in tube representation. Important binding pocket residues are shown as sticks and colored according to charge: negative (red), positive (blue), and neutral (orange). The backbone amide carbon atom of each residue is shown as a sphere to guide the eye. Hydrogens are omitted for clarity.

Artificially removing the native ligand ADP·Mg^{2+} cation reduced the computed binding energy by ~60%, similarly for the ellipticine competitor ligand with binding energies reduced by ~40% upon artificially constraining N2 to its unprotonated state. Note that in the less favorable orientation **E** (Figure 3, based on ref *19*) with the N2 site less "buried" in the pocket and more exposed to solvent the reduction in binding energy associated with N2 deprotonation is only ~10%.

Similar charge balancing, in both the ligand and protein binding pocket, for the optimization of ligand binding affinity and specificity has been previously noted for other proteins; see, for example, refs *30* and *31* and references cited within. Indeed, the link between protein binding pocket structural stability and highly coupled electrostatic networks is a major obstacle for the design of active mutant proteins "reengineered" for novel ligand recognition, as described in ref *34*. As discussed below, the strong N2-H^+−Glu640 ellipticine−c-kit interaction and consequent "nucleotide-type" inhibitor binding mode identified in the present study has dramatic consequences for the design of ADP/ATP analogues that target mutant c-kit and may be active against malignant cancers.

Possible Routes to Enhanced Ellipticine Derivative Inhibition of c-kit Tyrosine Kinase. The most important short to medium term consequence of the "nucleotide-type" binding mode identified in the present study for ellipticine-based inhibitors is for the development of more active inhibitors utilizing the structure of well-known kinase inhibitors of type **2A** and **2B** in Figure 1, e.g., indolocarbazoles and phenylpyrrolocarbazoles. The novel "nucleotide-type" binding mode means a radical rethink of inhibitor design, with the space for derivitization orientated from C4/C5 of ellipticine ligand **1** in Figure 1. The novel predicted binding mode is based on the computed strong preference for ellipticine N2 protonation in c-kit and consequent strong electrostatic contact between N2-H^+ and the binding pocket, principally Glu640, and further supported by the calculated binding specificities for ligand **1** relative to the carboxamide derivatives **8** and **10** in Figure 2. We are currently testing these predictions experimentally and will continue to use a combined, highly integrated simulation/experiment approach to design optimum inhibitor molecules for the mutant c-kit pocket.

A central question for the eventual use of ellipticine-based pharmacores as anticancer drugs is their promiscuity (*64*) in vivo, that is, the potential of the c-kit inhibitor to bind to other biomolecules including closely related kinase enzymes and cause unwanted side interactions and drug toxicity (*65*−*67*). One very promising approach is to design inhibitors that not only exploit small, sequence and conformational kinase binding pocket variations but also target distinct kinase conformations, e.g., STI-571 binding to inactive c-kit (*58*) and ellipticine binding to active c-kit (*19*).

The present study uses a combination of simulation techniques based on molecular dynamics and free energy calculations to design optimum active c-kit inhibitors, and the very detailed atom-scale binding dynamics and binding free energy data produced are currently being tested by us using experimental binding assays. The data could also be used to "validate" faster, less rigorous binding calculations for an extensive computational screening of multiple inhibitor−kinase interactions, e.g., along the lines of ref *67*, providing insight into the sometimes counterintuitive experimental binding data (*65, 66*).

CONCLUSIONS

Computational Drug Design as Support for Experiment. X-ray crystal structures (where available) and kinetic binding experiments provide a wealth of information on ligand−protein complexation including inhibitor−receptor interactions, allowing identification of binding sites and in many cases the determination of binding constants and binding free energies, crucial for the design of novel inhibitor drug molecules. Computer simulations provide a valuable aid, allowing insight into the structure, dynamics, and energetics of binding (*19, 22*−*35, 49*−*,62*−*64*). By alchemically mutating from one state to the other, it is possible to rigorously compute the binding free energy difference between similar sized ligands with similar binding modes (*28*−*34*). Furthermore, binding pocket groups contributing strongly to ligand binding specificity may be identified. Indeed, we show here the power of MDFE calculations to reproduce experimental binding rank orders (*19*) for a series of ellipticine-based compounds binding to c-kit tyrosine kinase (with one exception as discussed), and extensive sampling of a range of ligand orientations and calculation of pK_a shifts indentified a novel nucleotide-type binding geometry that provides significantly enhanced inhibitor binding. The relative contributions of c-kit binding pocket groups to binding specificities were calculated and rationalized from the MD structures, providing leads for the design of more potent anticancer c-kit inhibitors, namely, ellipticine-based compounds functionalized at the C4/C5 region.

The ability to functionalize both ligand and enzyme structures for the rational design of novel inhibitor−receptor complexes is central to the development of more active, less toxic drugs. Computer simulations can speed up this costly and difficult task by highlighting the most important contributors to binding specificity, and in the absence of crystal structures, simulations (*19, 34, 40, 59, 62, 63, 68*) can be used to identify binding orientations consistent with kinetic data.

SUPPORTING INFORMATION AVAILABLE

MD structures for ligand **1** binding in orientations **B** and **C** in charged/neutral states and in orientations **D** and **E** in the neutral state, control simulations for an ellipticine derivative (ligand **11**) with the pyridine moiety replaced by a phenyl group, MD structures for ligands **3**−**6** binding in orientation **A**, MD structures for ligand **6** binding in orientations **D** and **E**, and generated CHARMM force field parameters for the ellipticine series of compounds. This material is available free of charge via the Internet at http://pubs.acs.org.

REFERENCES

1. Schlessinger, J. (2000) Cell signaling by receptor tyrosine kinases. *Cell 103*, 211–225.
2. Ashman, L. K. (1999) The biology of stem cell factor and its receptor c-kit. *Int. J. Biochem. Cell Biol. 31*, 1037–1051.
3. Linnekin, D. (1999) Early signaling pathways activated by c-kit in hematopoietic cells. *Int. J. Biochem. Cell Biol. 31*, 1053–1074.
4. Edling, C. E., and Hallberg, B. (2007) c-kit—a hematopoietic cell essential receptor tyrosine kinase. *Int. J. Biochem. Cell Biol. 39*, 1995–1998.
5. Lev, S., Blechman, J. M., Givol, D., and Yarden, Y. (1994) Steel factor and c-kit protooncogene: genetic lessons in signal transduction. *Crit. Rev. Oncog. 5*, 141–168.
6. Duensing, A., Madeiros, F., McConarty, B., Joseph, N. E., Panigrahy, D., Singer, S., Demetri, G. D., Fletcher, C. D. M., and Fletcher, J. A. (2004) Mechanisms of oncogenic KIT signal transduction in primary gastrointestinal stromal tumors (GISTs). *Oncogene 23*, 3999–4006.
7. Vogelstein, B., and Kinzler, K. W. (2004) Cancer genes and the pathways they control. *Nat. Med. 10*, 789–799.
8. Chian, R., Young, S., Danilkovitch-Miagkova, A., Ronnstrand, L., Leonard, E., Ferrao, P., Ashman, L., and Linnekin, D. (2001) Expression of constitutively activated human c-kit in Myb transformed early myeloid cells leads to factor independence, histiocytic differentiation, and tumorigenicity. *Blood 98*, 1365–1373.
9. Ma, Y., Zeng, S., Metcalfe, D. D., Akin, C., Dimitrijevic, S., Butterfield, J. H., McMahon, G., and Longley, B. J. (2002) The c-kit mutation causing human mastocytosis is resistant to STI571 and other KIT kinase inhibitors kinases with enzymatic site mutations show different inhibitor sensitivity profiles than wild-type kinases and those with regulatory-type mutations. *Blood 99*, 1741–1744.
10. Attoub, S., Rivat, C., Rodrigues, S., Van Bocxlaer, S., Bedin, M., Bruyneel, E., Louvet, C., Kornprobst, M., Andre, T., Mareel, M., Mester, J., and Gespach, C. (2002) The c-kit tyrosine kinase inhibitor STI571 for colorectal cancer therapy. *Cancer Res. 62*, 4879–4883.
11. Looijenga, L. H., de Leeuw, H., van Oorschot, M., van Gurp, R. J., Stoop, H., Gillis, A. J., de Gouveia Brazao, C. A., Weber, R. F., Kirkels, W. J., van Dijk, T., et al. (2003) Stem cell factor receptor (c-kit) codon 816 mutations predict development of bilateral testicular germ-cell tumors. *Cancer Res. 63*, 7674–7678.
12. Corbin, A. S., Griswold, I. J., La Rose, P., Yee, K. W., Heinrich, M. C., Reimer, C. L., Druker, B. J., and Deininger, M. W. (2004) Sensitivity of oncogenic KIT mutants to the kinase inhibitors MLN518 and PD180970. *Blood 104*, 3754–3757.
13. Dibb, N. J., Dilworth, S. M., and Mol, C. D. (2004) Switching on kinases: oncogenic activation of BRAF and the PDGFR family. *Nat. Rev. Cancer 4*, 718–727.
14. Growney, J. D., Clark, J. J., Adelsperger, J., Stone, R., Fabbro, D., Griffin, J. D., and Gilliland, D. G. (2005) Activation mutations of human c-kit resistant to imatinib mesylate are sensitive to the tyrosine kinase inhibitor PKC412. *Blood 106*, 721–724.
15. Akin, C. (2006) Molecular diagnosis of mast cell disorders: a paper from the 2005 William Beaumont Hospital symposium on molecular pathology. *J. Mol. Diagn. 8*, 412–419.
16. Young, S. M., Cambareri, A. C., and Ashman, L. K. (2006) Role of c-kit expression level and phosphatidylinositol 3-kinase activation in survival and proliferative responses of early myeloid cells. *Cell Signalling 18*, 608–620.
17. Webster, J. D., Kiupel, M., and Yuzbasiyan-Gurkan, V. (2006) Evaluation of the kinase domain of c-kit in canine cutaneous mast cell tumors. *BMC Cancer 6*, 85.
18. Roberts, K. G., Odell, A. F., Byrnes, E. M., Baleato, R. M., Griffith, R., Lyons, A. B., and Ashman, L. K. (2007) Resistance to c-kit kinase inhibitors conferred by V654A mutation. *Mol. Cancer Ther. 6*, 1159–1166.
19. Vendome, J., Letard, S., Martin, F., Svinarchuk, F., Dubreuil, P., Auclair, C., and Le Bret, M. (2005) Molecular modeling of wild type and D816V c-kit inhibition based on ATP competitive binding of ellipticine derivatives to tyrosine kinases. *J. Med. Chem. 48*, 6194–6201.
20. Manez, S., and Del Carmen Recio, M. (2002) Bioactive Natural Products, in *Studies in Natural Products Chemistry* (Atta-ur-Rahman, Ed.) Vol. 27, pp 819−890, Elsevier Science Publishers BV, Amsterdam, The Netherlands.
21. Booth, R. J., Denny, W. A., Dobrusin, E. M., Kraker, A. J., Mitchell, L. H., Smaill, J. B., Thompson, A. M., Lee, H. H., McCarthy, F. O. J., and Palmer, B. D. (2003)PCT International Patent WO 03/091255.
22. Wong, C., and McCammon, J. (1986) Dynamics and design of enzymes and inhibitors. *J. Am. Chem. Soc. 108*, 3830–3832.
23. Warshel, A., Sussman, F., and King, G. (1986) The free energies of charges in solvated proteins. Microscopic calculations using a reversible charging process. *Biochemistry 25*, 8368–8372.
24. Warshel, A. (1991) *Computer modelling of chemical reactions in enzymes and solutions*, John Wiley and Sons, New York.
25. Kollman, P. (1993) Free energy calculations—applications to chemical and biochemical phenomena. *Chem. Rev. 93*, 2395–2417.
26. van Gunsteren, W., Beutler, T., Fraternali, F., King, P., Mark, A., and Smith, P. (1993) in *Computer simulation of biomolecular systems* (van Gunsteren, W., Weiner, P., and Wilkinson, A. Eds.) pp 315−348, Escom Science Publishers, Leiden, The Netherlands.
27. Lamb, M. L., and Jorgensen, W. (1997) Computational approaches to molecular recognition. *Curr. Opin. Chem. Biol. 1*, 449–457.
28. Simonson, T. (2001) in *Computational Biochemistry and Biophysics* (Becker, O. M., MacKerell, A. D., Roux, B., and Watanabe, M. Eds.) pp 169−197, Marcel Dekker, New York.
29. Simonson, T., Archontis, G., and Karplus, M. (2002) Free energy simulations come of age: protein-ligand recognition. *Acc. Chem. Res. 35*, 430–437.
30. Thompson, D., Plateau, P., and Simonson, T. (2006) Free energy simulations and experiments reveal long-range electrostatic interactions and substrate-assisted specificity in an aminoacyl-tRNA synthetase. *ChemBioChem 7*, 337–344.
31. Thompson, D., and Simonson, T. (2006) Molecular dynamics simulations show that bound Mg^{2+} contributes to amino acid and aminoacyl adenylate binding specificity in aspartyl-tRNA synthetase through long range electrostatic interactions. *J. Biol. Chem. 281*, 23792–23803.
32. Thompson, D., and Larsson, J. A. (2006) Modelling competitive guest binding to beta-cyclodextrin molecular printboards. *J. Phys. Chem. B 110*, 16640–16645.
33. Thompson, D., Lazennec, C., Plateau, P., and Simonson, T. (2007) Ammonium scanning in an enzyme active site: the chiral specificity of aspartyl-tRNA synthetase. *J. Biol. Chem. 282*, 30856–30868.
34. Thompson, D., Lazennec, C., Plateau, P., and Simonson, T. (2008) Probing electrostatic interactions and ligand binding in aspartyl-tRNA synthetase through site-directed mutagenesis and computer simulations. *Proteins: Struct., Funct., Bioinf. 71*, 1450–1460.
35. Wang, J., Deng, Y., and Roux, B. (2006) Absolute binding free energy calculations using molecular dynamics simulations with restraining potentials. *Biophys. J. 91*, 2798–2814.
36. Kraulis, P. J. (1991) Molscript: a program to produce both detailed and schematic plots of protein structures. *Appl. Crystallogr. 24*, 946–950.

37. Merritt, E. A., and Murphy, M. E. P. (1994) Raster3D version 2.0. A program for photorealistic molecular graphics. *Acta Crystallogr. D50*, 869–873.
38. Mol, C. D., Lim, K. B., Sridhar, V., Zou, H., Chien, E. Y. T., Sang, B.-C., Nowakowski, J., Kassel, D. B., Cronin, C. N., and McRee, D. E. (2003) Structure of a c-kit product complex reveals the basis for kinase transactivation. *J. Biol. Chem. 278*, 31461–31464.
39. Archontis, G., Simonson, T., and Karplus, M. (2001) Binding free energies and free energy components from molecular dynamics and Poisson-Boltzmann calculations. Application to amino acid recognition by aspartyl-tRNA synthetase. *J. Mol. Biol. 306*, 307–327.
40. Archontis, G., Simonson, T., Moras, D., and Karplus, M. (1998) Specific amino acid recognition by aspartyl-tRNA synthetase studied by free energy simulations. *J. Mol. Biol. 275*, 823–846.
41. Beglov, D., and Roux, B. (1994) Finite representation of an infinite bulk system: solvent boundary potential for computer simulations. *J. Chem. Phys. 100*, 9050–9063.
42. Brooks, B. R., Bruccoleri, R. E., Olafson, B. D., States, D. J., Swaninathan, S., and Karplus, M. (1983) CHARMM: A program for macromolecular energy, minimization, and dynamics calculations. *J. Comput. Chem. 4*, 187–217.
43. MacKerell, A. D., Bashford, D., Bellott, M., Dunbrack, D. L., Evanseck, J. D., Field, M. J., Fischer, S., Gao, J., Guo, H., Ha, S., Joseph-McCarthy, D., Kuchnir, L., Kuczera, K., Lau, F. T. K., Mattos, C., Michnick, S., Ngo, T., Nguyen, D. T., Prodhom, B., III, Roux, B., Schlenkrich, M., Smith, J., Stote, R., Straub, J., Watanabe, M., Wiórkiewicz-Kuczera, J., Yin, D., and Karplus, M. (1998) All-atom empirical potential for molecular modeling and dynamics studies of proteins. *J. Phys. Chem. B 102*, 3586–3616.
44. Frisch, M. J., Trucks, G. W., Schlegel, H. B., Scuseria, G. E., Robb, M. A., Cheeseman, J. R., Montgomery, J. A., Jr., Vreven, T., Kudin, K. N., Burant, J. C., Millam, J. M., Iyengar, S. S., Tomasi, J., Barone, V., Mennucci, B., Cossi, M., Scalmani, G., Rega, N., Petersson, G. A., Nakatsuji, H., Hada, M., Ehara, M., Toyota, K., Fukuda, R., Hasegawa, J., Ishida, M., Nakajima, T., Honda, Y., Kitao, O., Nakai, H., Klene, M., Li, X., Knox, J. E., Hratchian, H. P., Cross, J. B., Bakken, V., Adamo, C., Jaramillo, J., Gomperts, R., Stratmann, R. E., Yazyev, O., Austin, A. J., Cammi, R., Pomelli, C., Ochterski, J. W., Ayala, P. Y., Morokuma, K., Voth, G. A., Salvador, P., Dannenberg, J. J., Zakrzewski, V. G., Dapprich, S., Daniels, A. D., Strain, M. C., Farkas, O., Malick, D. K., Rabuck, A. D., Raghavachari, K., Foresman, J. B., Ortiz, J. V., Cui, Q., Baboul, A. G., Clifford, S., Cioslowski, J., Stefanov, B. B., Liu, G., Liashenko, A., Piskorz, P., Komaromi, I., Martin, R. L., Fox, D. J., Keith, T., Al-Laham, M. A., Peng, C. Y., Nanayakkara, A., Challacombe, M., Gill, P. M. W., Johnson, B., Chen, W., Wong, M. W., Gonzalez, C., and Pople, J. A. (2004) Gaussian 03, revision C.02, Gaussian, Inc., Wallingford, CT.
45. Becke, A. D. (1993) Density-functional thermochemistry. III. The role of exact exchange. *J. Chem. Phys. 98*, 5648–5652.
46. Reed, A. E., Weinstock, R. B., and Weinhold, F. (1985) Natural population analysis. *J. Chem. Phys. 83*, 735–746.
47. Jorgensen, W., Chandrasekar, J., Madura, J., Impey, R., and Klein, M. (1983) Comparison of simple potential functions for simulating liquid water. *J. Chem. Phys. 79*, 926–935.
48. Ryckaert, J. P., Ciccotti, G., and Berendsen, H. J. C. (1977) Molecular dynamics of n-alkanes. *J. Comput. Phys. 23*, 327–341.
49. Fernandez, A., Sanguino, A., Peng, Z., Ozturk, E., Chen, J., Crespo, A., Wulf, S., Shavrin, A., Qin, C., and Ma, J. (2007) An anticancer c-kit kinase inhibitor is reengineered to make it more active and less cardiotoxic. *J. Clin. Invest. 117*, 4044–4054.
50. Archontis, G., and Simonson, T. (2005) Proton binding to proteins: a self-consistent dielectric continuum analysis. *Biophys. J. 88*, 3888–3904.
51. Archontis, G., and Simonson, T. (2001) Dielectric relaxation in an enzyme active site: molecular dynamics simulations interpreted with a macroscopic continuum model. *J. Am. Chem. Soc. 123*, 11047–11056.
52. Im, W., Beglov, D., and Roux, B. (1998) Continuum solvation model: electrostatic forces from numerical solutions to the Poisson-Boltzmann equation. *Comput. Phys. Commun. 111*, 59–75.
53. Yang, A.-S., and Honig, B. (1993) On the pH dependence of protein stability. *J. Mol. Biol. 231*, 459–474.
54. Alexov, E. G., and Gunner, M. R. (1997) Incorporating protein conformational flexibility into the calculation of pH-dependent protein properties. *Biophys. J. 72*, 2075–2093.
55. Simonson, T. (2000) Electrostatic free energy calculations for macromolecules: a hybrid molecular dynamics/continuum electrostatics approach. *J. Phys. Chem. B 104*, 6509–6513.
56. Boresch, S., Archontis, G., and Karplus, M. (1994) Free-energy simulations-the meaning of the individual contributions from a component analysis. *Proteins: Struct., Funct., Genet. 20*, 25–33.
57. Boresch, S., and Karplus, M. (1995) The meaning of component analysis: decomposition of the free energy in terms of specific interactions. *J. Mol. Biol. 254*, 801–807.
58. Mol, C. D., Dougan, D. R., Schneider, T. R., Skene, R. J., Kraus, M. L., Scheibe, D. N., Snell, G. P., Zou, H., Sang, B.-C., and Wilson, K. P. (2004) Structural basis for the autoinhibition and STI-571 inhibition of c-kit tyrosine kinase. *J. Biol. Chem. 279*, 31655–31663.
59. Foster, R., Griffith, R., Ferrao, P., and Ashman, L. (2004) Molecular basis of the constitutive activity and STI571 resistance of Asp816Val mutant KIT receptor tyrosine kinase. *Mol. Graphics Model. 23*, 139–152.
60. Schmitt, E., Moulinier, L., Fujiwara, S., Imanaka, T., Thierry, J. C., and Moras, D. (1998) Crystal structure of aspartyl-tRNA synthetase from Pyrococcus kodakaraensis KOD: archaeon specificity and catalytic mechanism of adenylate formation. *EMBO J. 17*, 5227–5237.
61. Schwaller, M.-A., Allard, B., Lescot, E. , and Moreau, F. (1995) Protonophoric activity of ellipticine and isomers across the energy-transducing membrane of mitochondria. *J. Biol. Chem. 270*, 22709–22713.
62. Krystal, G. W., Honsawek, S., Kiewlich, D., Liang, C., Vasile, S., Sun, L., McMahon, G., and Lipson, K. E. (2001) Indolinone tyrosine kinase inhibitors block Kit activation and growth of small cell lung cancer cells. *Cancer Res. 61*, 3660–3668.
63. McLean, S. R., Gana-Weisz, M., Hartzoulakis, B., Frow, R., Whelan, J., Selwood, D., and Boshoff, C. (2005) Imatinib binding and cKIT inhibition is abrogated by the cKIT kinase domain I missense mutation Val654Ala. *Cancer Ther. 4*, 2008–2015.
64. Radhakrishnan, M. L., and Tidor, B. (2007) Specificity in molecular design: a physical framework for probing the determinants of binding specificity and promiscuity in a biological environment. *J. Phys. Chem. B 111*, 13419–13435.
65. Fabian, M. A., Biggs, W. H., III, Trieber, D. K., Atteridge, C. E., Azimioara, M. D., Benedetti, M. G., Carter, T. A., Ciceri, P., Edeen, P. T., Floyd, M., et al. (2005) A small molecule-kinase interaction map for clinical kinase inhibitors. *Nat. Biotechnol. 23*, 329–336.
66. Scapin, G. (2006) Protein kinase inhibition: different approaches to selective inhibitor design. *Curr. Drug Targets 7*, 1443–1454.
67. Chen, J., Zhang, X., and Fernandez, A. (2007) Molecular basis for specificity in the druggable kinome: sequence-based analysis. *Bioinformatics 23*, 563–572.
68. Zhang, D., Vaidehi, N., Goddard, W. A., Danzer, J., and Debe, D. (2002) Structure-based design of mutant Methanococcus jannaschii tyrosyl-tRNA synthetase for incorporation of O-methyl-L-tyrosine. *Proc. Natl. Acad. Sci. U.S.A. 99*, 6579–6584.

BI801239U